Chemical Engineering Journal 384 (2020) 123268

Contents lists available at ScienceDirect

Chemical Engineering Journal

journal homepage: www.elsevier.com/locate/cej

Surface sulfidization of spinel $LiNi_{0.5}Mn_{1.5}O_4$ cathode material for enhanced electrochemical performance in lithium-ion batteries

Luya Wei[a,b,1], Jianming Tao[a,1], Yanmin Yang[a], Xinyue Fan[a], Xinxin Ran[a], Jiaxin Li[a], Yingbin Lin[a,b,*], Zhigao Huang[a,b]

[a] College of Physics and Energy, Fujian Normal University, Fujian Provincial Solar Energy Conversion and Energy Storage Engineering Technology Research Center, Fuzhou 350117, China

[b] Fujian Provincial Collaborative Innovation Center for Optoelectronic Semiconductors and Efficient Devices, Xiamen 361005, China

HIGHLIGHTS

- Surface-sulfidized $LiNi_{0.5}Mn_{1.5}O_4$ exhibits capacity retention of 74.9% at 2 C after 2500 cycles.
- 3D porous structure of sulfidized-layer helps to form a stable SEI film.
- The reduced work function helps to enhance interfacial stability and cycling capability.
- SO_4^{2-}-adsorption suppresses Mn dissolution and enhances structural stability.

GRAPHICAL ABSTRACT

Surface-sulfidized $LiNi_{0.5}Mn_{1.5}O_4$ composites are synthesized through electrostatic interactions. Significant improvement in rate performance, cycling stability and thermal stability has been achieved in surface-sulfidized $LiNi_{0.5}Mn_{1.5}O_4$. A discharge capacity of 93.4 mAh g^{-1} can be still delivered at 2 C after 2500 cycles, with capacity retention of 74.9%. 3D sulfidized-layer with smaller work function helps to form a more stable CEI film on $LiNi_{0.5}Mn_{1.5}O_4$ surface, facilitates lithium-ions diffusion kinetics and enhances $LiNi_{0.5}Mn_{1.5}O_4$/electrolyte interfacial stability.

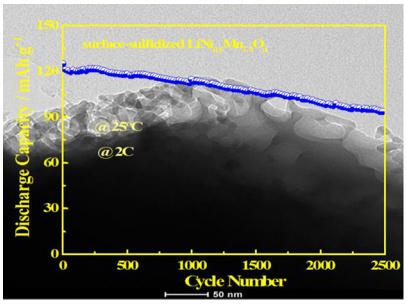

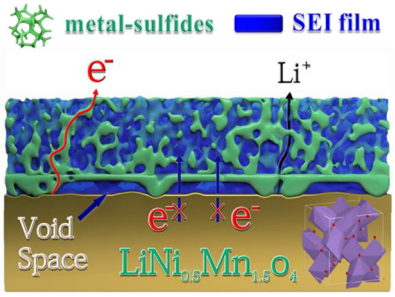

ARTICLE INFO

Keywords:
Lithium-ion batteries
$LiNi_{0.5}Mn_{1.5}O_4$
Surface-sulfidization
Diffusion coefficient
Work function

ABSTRACT

Stable interfacial structure is crucial for achieving superior electrochemical performances of high-voltage cathode materials for lithium-ion batteries. Herein, surface-sulfidized $LiNi_{0.5}Mn_{1.5}O_4$ cathode materials are synthesized through electrostatic interactions between positively-charged $LiNi_{0.5}Mn_{1.5}O_4$ and negatively-charged sulphur ion. A significant improvement in the rate capability, cycling stability and thermal stability has been achieved in surface-sulfidized $LiNi_{0.5}Mn_{1.5}O_4$ electrode. A discharge capacity of 93.4 mAh g^{-1} can be still delivered at 2 C after 2500 cycles with a capacity retention of 74.9%, which is far beyond that of the pristine one (45.3% after 1800 cycles). 3D porous structure of sulfidized-layer helps to form a stable cathode electrolyte interphase (CEI) film on $LiNi_{0.5}Mn_{1.5}O_4$ surface via accommodating interfacial strain between active materials and CEI film. Metal-sulfides on $LiNi_{0.5}Mn_{1.5}O_4$ surface could facilitate electron transfer across the $LiNi_{0.5}Mn_{1.5}O_4$/electrolyte interface, reduce charge transfer resistance and consequently enhance rate capability. The adsorption of SO_4^{2-} on $LiNi_{0.5}Mn_{1.5}O_4$ surface also helps to enhance $LiNi_{0.5}Mn_{1.5}O_4$/electrolyte interfacial stability. Moreover, the reduced work function induced by surface-sulfidization is considered to suppress

* Corresponding author at: College of Physics and Energy, Fujian Normal University, Fujian Provincial Solar Energy Conversion and Energy Storage Engineering Technology Research Center, Fuzhou 350117, China.
E-mail address: yblin@fjnu.edu.cn (Y. Lin).

[1] Equally contributed to this work.

https://doi.org/10.1016/j.cej.2019.123268
Received 5 August 2019; Received in revised form 15 October 2019; Accepted 21 October 2019
Available online 23 October 2019

decomposition of the electrolyte, improve interfacial stability and improve cycling stability. In terms of the superior electrochemical performances, surface-sulfidized $LiNi_{0.5}Mn_{1.5}O_4$ composites can be utilized as a promising cathode material for high-performance lithium ion batteries.

1. Introduction

Rechargeable lithium-ion batteries with high energy density have attracted increasing interest due to their commercial application in portable electronic devices, electric vehicles and large-scale energy storage [1,2]. The increasing demands for high-energy batteries make cathode materials with large specific energy be of primary concern [3,4]. Among the numerous cathode materials investigated so far, lithium nickel manganese oxide ($LiNi_{0.5}Mn_{1.5}O_4$) has received extensive attention because of its three-dimensional channels for fast Li^+ diffusion, high operation potential (~4.8 V *vs.* Li/Li^+) and relatively high theoretical capacity (148 mAh g^{-1}) [5,6]. Unfortunately, spinel $LiNi_{0.5}Mn_{1.5}O_4$ suffers from the aggressive oxidation of the electrolyte, Jahn-Teller distortion and the dissolution of transitional metals in the HF-containing electrolyte, leading in the structure deterioration and severe capacity fade upon cycling. To alleviate this problem mentioned above, lots of effective strategies have been developed such as nanostructure, doping with isovalent ions and surface modification [7–10]. Among approaches mentioned above, surface-coating has been considered as an effective way to improve electrochemical performances, which not only suppresses the formation of cathode electrolyte interphase (CEI) but also establishes a more stable interface to minimize side reactions. For example, Wang et al. [11] reported that Li_2SiO_3-coated $LiNi_{0.5}Mn_{1.5}O_4$ hollow spheres exhibited a superior cycling performance with capacity retention of 93.8% after 500 cycles at 25 °C at 1 C and 81.23% after 400 cycles at 50 °C at 1 C rate. Xu et al. [12] reported that YPO_4-coated $LiNi_{0.5}Mn_{1.5}O_4$ delivered a high capacity of 107mAh g^{-1} after 240 cycles with capacity retention of 77.5%, which was much higher than that of the pristine one.

However, most surface-coating materials are generally poor electronically conductive and incomplete coating on the active materials, resulting in poor kinetics during the insertion/extraction process and incomplete protection against HF attacking [13]. Up to now, many protective surface-coatings have been deposited on active material surface using various techniques including aqueous solution, solid-state reaction and sol-gel method. However, the lattice mismatch between $LiNi_{0.5}Mn_{1.5}O_4$ and coating-layer would cause poor Li-ion migration across the interface because of the increased energy barrier for hopping. On the other hand, the CEI film or surface-coating layer tends to peel off from $LiNi_{0.5}Mn_{1.5}O_4$ surface because of the strain repeatedly occurred

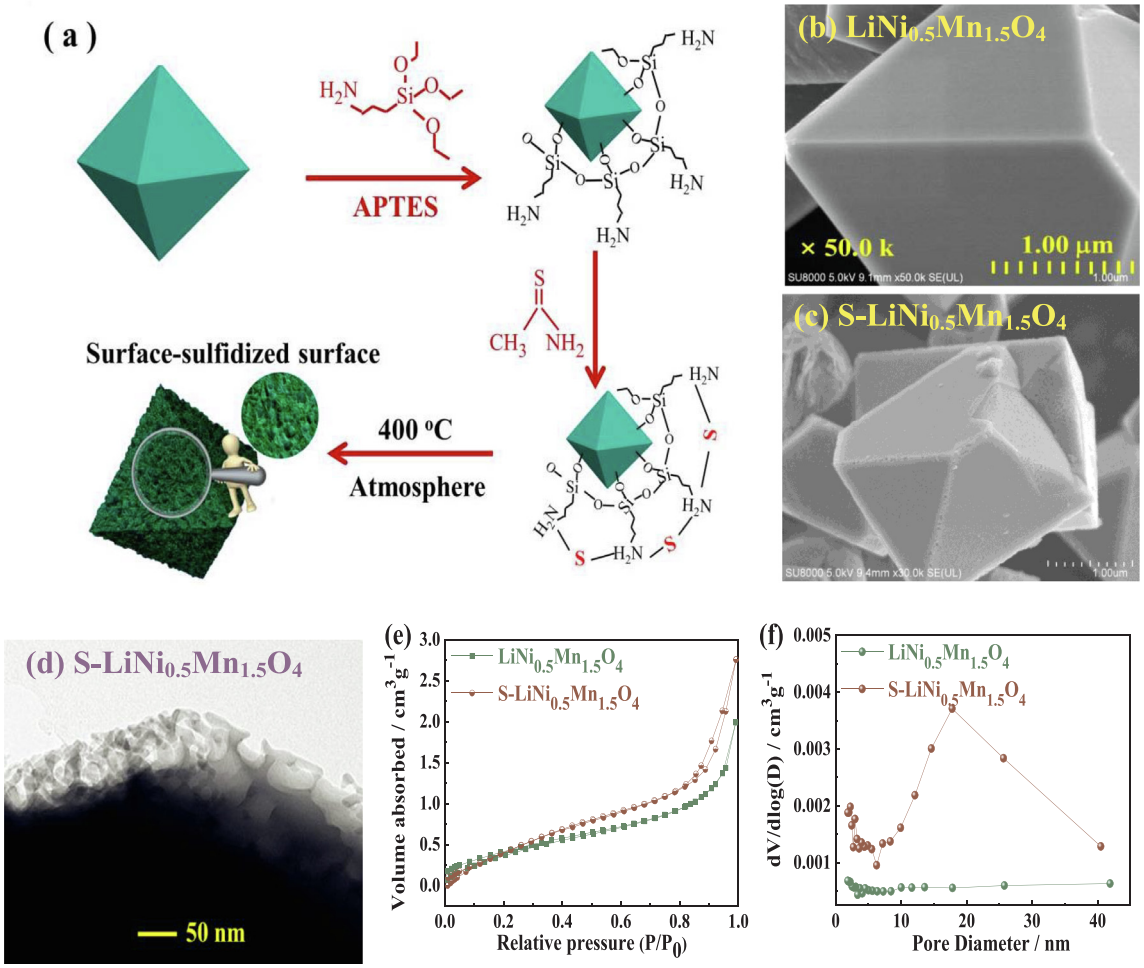

Fig. 1. (a) Schematic illustration of the preparation process for surface-sulfidized $LiNi_{0.5}Mn_{1.5}O_4$ powders. (b,c) SEM images of the as-prepared powders; (d) TEM image of surface-sulfidized $LiNi_{0.5}Mn_{1.5}O_4$ powders; (e, f) Nitrogen sorption isotherms and pore diameter distribution of $LiNi_{0.5}Mn_{1.5}O_4$ and surface-sulfidized $LiNi_{0.5}Mn_{1.5}O_4$ powders.

at the interfacial lattice-mismatch region especially when Li-ions hop through [14,15]. Therefore, three-dimensional (3D) structure with excellent conductivity should be highly desirable for surface-modification, which could not only protect active materials from HF-attacking, but also enhance the adhesion between the pristine cathode and CEI film.

In this work, surface-sulfidized $LiNi_{0.5}Mn_{1.5}O_4$ composites have been prepared via electrostatic interactions between surface-functionalized $LiNi_{0.5}Mn_{1.5}O_4$ and S^{2-} source. A porous framework with excellent conductivity has grown on $LiNi_{0.5}Mn_{1.5}O_4$ surface. Comparing to $LiNi_{0.5}Mn_{1.5}O_4$, surface-sulfidized $LiNi_{0.5}Mn_{1.5}O_4$ exhibits the superior electrochemical performances especially in terms of the long-term cyclic stability and thermal stability.

2. Experimental

2.1. Preparation of cathode materials

Spinel $LiNi_{0.5}Mn_{1.5}O_4$ cathode materials are prepared by a sol-gel method using tartaric acid as a chelating agent. All the chemicals are of analytical grade and used without further purification. In a typical process, 8.1 g $CH_3COOLi{\cdot}2H_2O$, 2.7 g $Ni(CH_3COO)_2{\cdot}4H_2O$ and 2.3 g $Mn(CH_3COO)_2{\cdot}6H_2O$ are dissolved in de-ionized water with 3% excess of $LiCH_3COO{\cdot}2H_2O$ to compensate the loss of lithium element during high temperature calcination. Then, 13.2 g tartaric acid is added to the mixing solution, in which the molar ratio of tartaric acid to total metal ions was 2:1. The aqueous solution is kept stirring at 90 °C until a viscous blue gel is obtained. The resulting gel is further dried at 280 °C for 10 h and subsequently sintered at 500 °C in air atmosphere for 5 h to decompose the acetate components and organic constituents. Finally, the obtained precursor powders are calcinated at 900 °C in air for 12 h to obtain homogeneous $LiNi_{0.5}Mn_{1.5}O_4$ cathode materials.

Surface-sulfidization is carried out via electrostatic interactions between positively-charged $LiNi_{0.5}Mn_{1.5}O_4$ particles and negatively-charged sulphur ion in alcohol solution. Typically, 0.3 g $LiNi_{0.5}Mn_{1.5}O_4$ particles are dispersed in 200 mL absolute ethanol under ultrasonication for 60 min following by adding 1 mL 3-aminopropyltriethoxysilane (APTES). After vigorous stirring for 12 h, the resulted precipitates are collected by centrifugation and washed several times with ethanol to obtain amino-silane modified $LiNi_{0.5}Mn_{1.5}O_4$ nanoparticles. Then the amino-silane modified $LiNi_{0.5}Mn_{1.5}O_4$ particles are dispersed in 100 mL absolute ethanol under ultrasonication, followed by dropping stoichiometric amounts of thioacetamide (C_2H_5NS). The PH of the mixed solution is adjusted to 9.0 using aqueous ammonia and the negatively-charged sulfur ions are expected to strongly adsorb on the positively-charged $LiNi_{0.5}Mn_{1.5}O_4$ surface via electrostatic interactions. After reaction for 12 h, the precipitates are collected by centrifugation, washed with absolute ethanol several times and sintered at 400 °C in Ar atmosphere for 12 h to obtain surface-sulfidized $LiNi_{0.5}Mn_{1.5}O_4$ (denoted as S-$LiNi_{0.5}Mn_{1.5}O_4$ in the following text). Schematic illustrations of preparation process of surface-sulfidized $LiNi_{0.5}Mn_{1.5}O_4$ is shown in Fig. 1(a).

2.2. Materials characterizations

The crystal structure of the as-prepared composites is characterized by X-ray diffractometry (XRD, Rigaku MinFlex II) with Cu-Kα radiation (λ = 0.15406 nm). The morphologies of the $LiNi_{0.5}Mn_{1.5}O_4$ and S-$LiNi_{0.5}Mn_{1.5}O_4$ are investigated by field-emission scanning electron microscopy (FESEM; HITACHI, SU-8010) equipped with an energy-dispersive spectroscopy (EDS) and transmission electron microscopy (TEM, Tecnai G2 F20 S-TWIN). Nitrogen sorption isotherms at 77 K are measured using a Micromeritics Tristar 3020 analyzer and the pore size distribution is determined according to the theory of Barrett Joyner and Halenda (BJH). The surface chemistry is analyzed by X-ray photoelectron spectroscopy (XPS, ESCALAB 250 Xi, USA). The surface potentials of the as-prepared composites are characterized by Kelvin probe atomic force microscopy (KPAFM) (Bruker dimension ICON, Germany).

2.3. Electrochemical measurements

The electrochemical performances of $LiNi_{0.5}Mn_{1.5}O_4$ and S-$LiNi_{0.5}Mn_{1.5}O_4$ cathode materials are evaluated with CR2025-type coin cell using lithium foil as a counter electrode. The cathode slurry is prepared by mixing 80 wt% active material ($LiNi_{0.5}Mn_{1.5}O_4$ or S-$LiNi_{0.5}Mn_{1.5}O_4$) with 10 wt% super-P and 10 wt% polyvinylidene fluoride (PVDF) in a solvent (N-methy1-2-pyrrolidone), which is cast onto an aluminum foil and subsequently dried at 110 °C in vacuum for 12 h. The loading density of the active materials is ~2.2 $mg{\cdot}cm^{-2}$. Electrochemical cells are assembled in an argon-filled glove box with O_2 and H_2O content below 1 ppm, using a microporous polypropylene membrane (Celgard 2400) as a separator and 1 M $LiPF_6$ in ethylene carbonate (EC)-dimethyl carbonate (DMC) (1:1 in volume) as the electrolyte. The galvanostatic charge/discharge tests are carried out in the voltage range of 3.0 and 4.9 V (*vs.* Li^+/Li) on a LAND battery testing system (LAND CT2001A). Electrochemical impedance spectra of the cells are recorded on a Zahner Zennium IM6 electrochemical workstation in the frequency range of 10 mHz to 100 kHz with AC amplitude of 5 mV. Thermal stability of the as-prepared samples is evaluated with differential scanning calorimetry (DSC) technique on a TG-DSC simultaneous thermal analyzer (Netzsch STA449F3) in a temperature range of 30–400 °C at a heating rate of 2 °C min^{-1}. Prior to DSC measurements, the cells are charged to 4.9 V at 0.1 C and then constant-voltage charged at 4.9 V for an additional 6 h, followed by disassembled in an argon-filled glove box to obtain charged cathode powder. The cathode materials including PVDF and Super-P are scraped from aluminum foil and subsequently sealed in a stainless-steel high-pressure pan for DSC measurements.

2.4. First principles density functional calculations

Density functional theory (DFT) calculations are carried out using the Vienna Ab initio Simulation Package (VASP) along with the projector augmented-wave method. The exchange correlation functional is depicted by Perdew-Burke-Ernzerhof (PBE) with generalized gradient approximation (GGA) functionals and the electron–ion interaction is described with the projector augmented wave (PAW) method. According to the work by Sun et al. [16], DFT + *U* approximation is employed to accurately describe the 3d orbitals for the transition metals, where *Ueff* is set as *U*(Mn) = 3.9 eV and *U*(Ni) = 6.2 eV respectively. For geometry optimizations, the 4 × 4 × 1 k-points in the Brillouin zone are used and the energy cutoff is 520 eV. A vacuum layer of 15 Å is added to avoid any interaction between adjacent surfaces. The lattice constants and atomic positions are fully relaxed until the Hellmann–Feynman forces acing on each atom are less than 0.02 eV/Å.

3. Results and discussion

3.1. Material characterizations

Fig. 1(b, c) presents the typical morphologies and microstructure of $LiNi_{0.5}Mn_{1.5}O_4$ and S-$LiNi_{0.5}Mn_{1.5}O_4$ samples. SEM images reveal that $LiNi_{0.5}Mn_{1.5}O_4$ has a clean and smooth surface while S-$LiNi_{0.5}Mn_{1.5}O_4$ demonstrates rough and porous surface, which is further confirmed by TEM image shown in Fig. 1(d). N_2 adsorption/desorption isotherms of S-$LiNi_{0.5}Mn_{1.5}O_4$ (Fig. 1(e)) show a typical type IV isotherm at relative pressure (P/P_0) between 0.8 and 1.0, indicating the existence of the mesoporous structure in S-$LiNi_{0.5}Mn_{1.5}O_4$ particle [17]. Fig. 1(f) shows the Barrett–Joyner–Halenda pore-size distribution of the as-prepared composites, revealing that S-$LiNi_{0.5}Mn_{1.5}O_4$ samples have larger average pore size (18 nm) while no pore-structure feature is observed in $LiNi_{0.5}Mn_{1.5}O_4$. The analysis of pore-size distribution is consistent with

TEM measurements.

The elemental distribution of the S-$LiNi_{0.5}Mn_{1.5}O_4$ surface is characterized using EDS mapping. In the selected region of Fig. 2(a-f), the element mapping of S is overlapped with that of Ni, Mn and O elements, indicating that surface-sulfidized layer is evenly coated on the pristine $LiNi_{0.5}Mn_{1.5}O_4$ surface. X-ray photoelectron spectroscopy measurements are performed to further clarify the oxidation states of Ni, Mn, O and S on the S-$LiNi_{0.5}Mn_{1.5}O_4$ surface. Two distinct peaks at 854.9 and 872.8 eV in the Ni *2p* core-level spectrum (Fig. 2(h)) are the characteristic peaks of Ni^{2+} and Ni^{3+} [18]. As shown in Fig. 2 (i), both Mn 2p3/2 and 2p1/2 peaks can be fitted into two split components of Mn^{3+} and Mn^{4+}. The peaks at 653.2 eV and 654.5 eV of the Mn 2p1/2 spectrum are assigned to Mn^{3+} and Mn^{4+}, and those at 642.0 and 643.5 eV for Mn^{3+} and Mn^{4+} in the Mn 2p3/2 spectrum [19]. In the S *2p* region (Fig. 2 (k)), several fitted peaks suggest complex reactions occur during the sulfidization process. The binding energies around 164.2 eV indicate typical metal-sulfide bonding in the bimetallic sulfide with bridging S_2^{2-} and/or apical S^{2-} [20], and the characteristic peak at ~68.9 eV could be assigned to sulphur ion species with a higher oxidation state such as metal–O–S species or adsorption of SO_4^{2-} [21]. The peaks at 102.1 eV in the Si *2p* spectrum is assigned to the Si *2p* in SiO_2 [22], indicating that the $LiNi_{0.5}Mn_{1.5}O_4$ surface is also coated by SiO_2 particles

The crystal structures of $LiNi_{0.5}Mn_{1.5}O_4$ and S-$LiNi_{0.5}Mn_{1.5}O_4$ are characterized by X-ray diffraction, shown in Fig. 3(a). All diffraction peaks of both samples are readily indexed to the typical structure of a spinel phase with a space group of Fd-3m [23] and the additional diffraction peak at 29.36° is assigned to MnS_2 phase (JCPDS no. 25-0549).

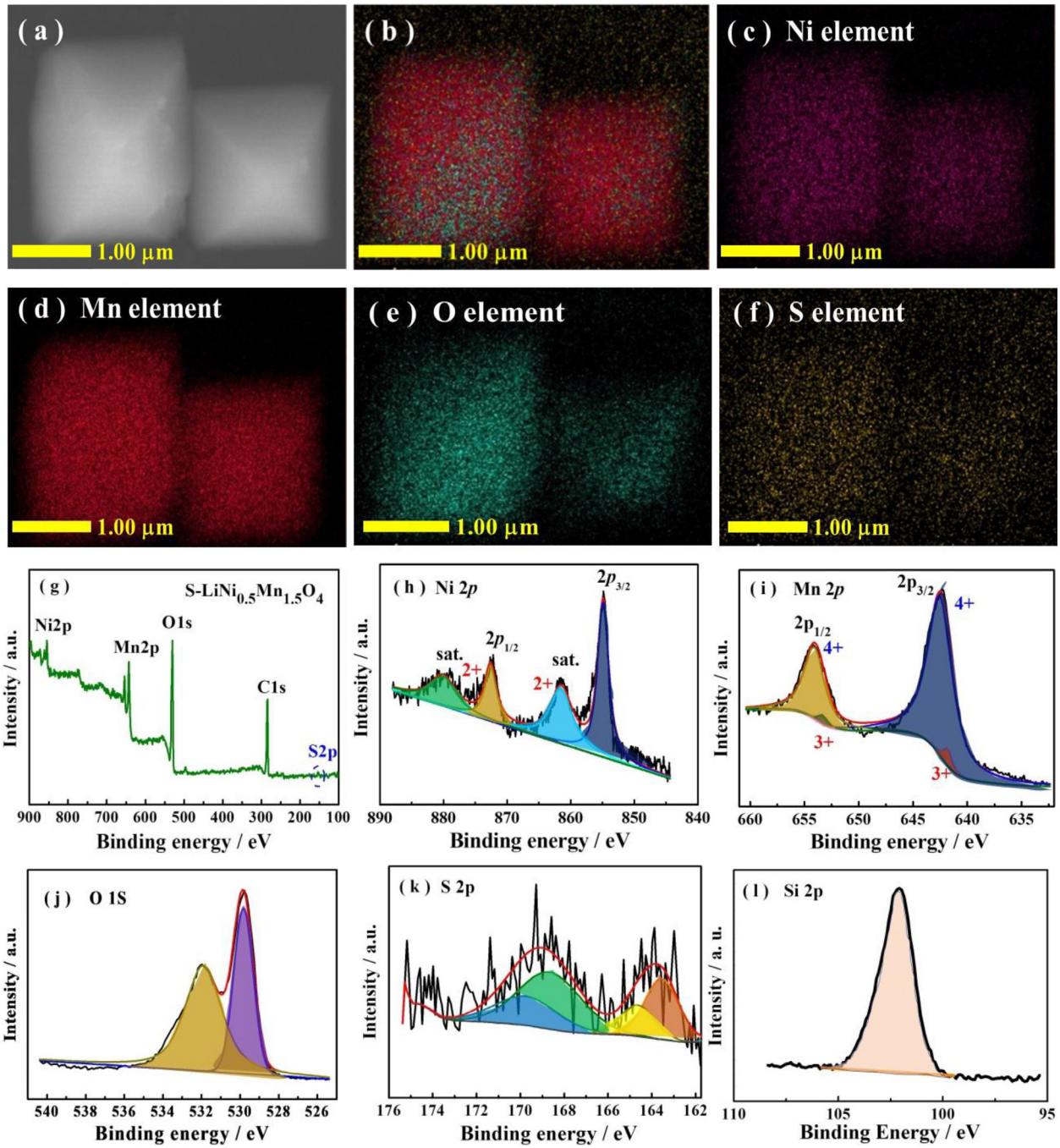

Fig. 2. (a-f) the EDS mapping images and (g-l) XPS spectra of the S-$LiNi_{0.5}Mn_{1.5}O_4$ composites.

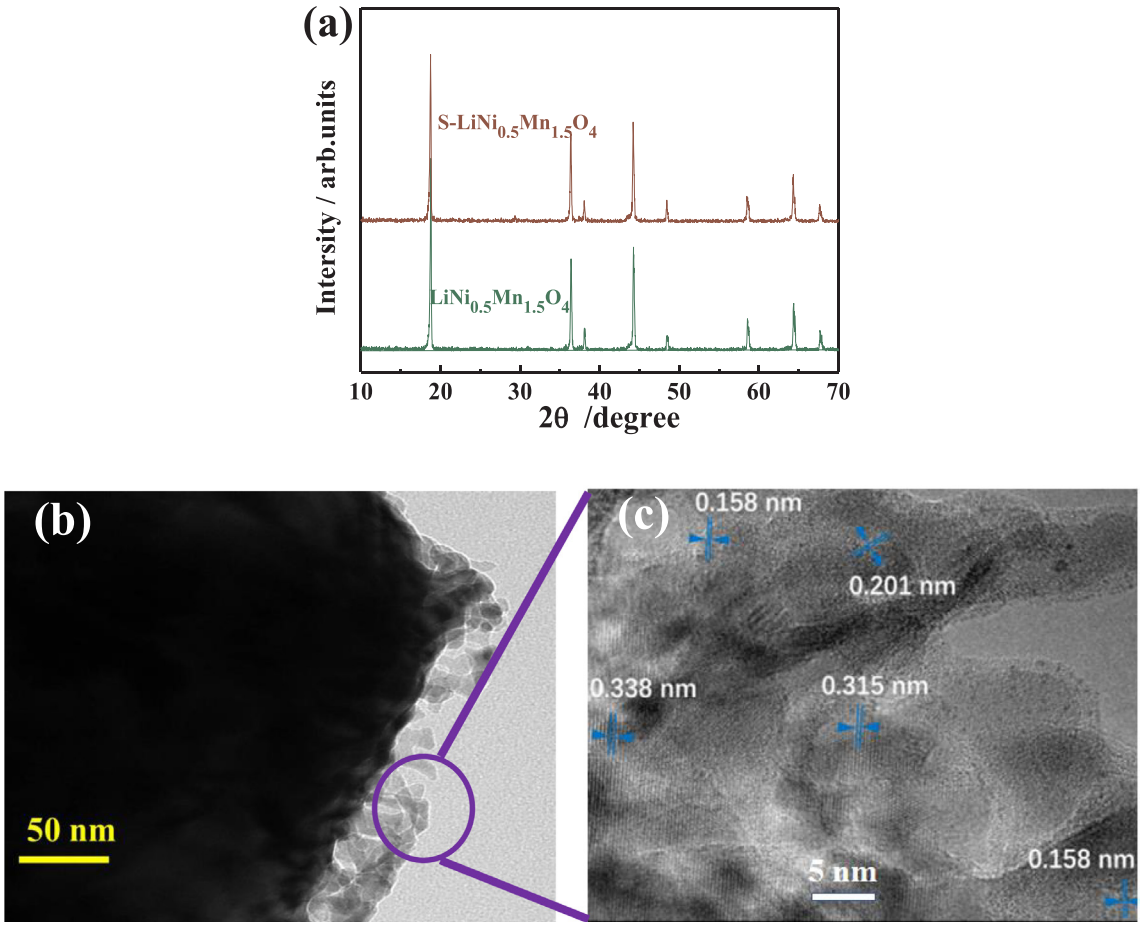

Fig. 3. (a) XRD patterns of the as-prepared samples; (b, c) TEM images of the S-$LiNi_{0.5}Mn_{1.5}O_4$ composite.

Fig. 3(c, d) presents the high-resolution TEM image of surface-sulfidized layer on $LiNi_{0.5}Mn_{1.5}O_4$ surface. The lattice spacing of 0.201 nm and 0.338 nm could be readily assigned to the (0 2 0) planes of Ni_3S_2 and the (2 2 0) planes of Ni_3S_4, respectively [24,25]. Interplanar distances of 0.315 nm corresponds to the (1 0 1) crystal planes of MnS with a wurtzite structure [26]. Such surface-sulfidized layer could mitigate side reactions via reducing immediate contact vicinity among active materials and simultaneously facilitates electron transfer in the electrode.

Based on the XRD, Raman, TEM and XPS measurements, the porous metal-sulfides framework on $LiNi_{0.5}Mn_{1.5}O_4$ surface could be formed as follows. Firstly, in the alkaline medium, CH_3CSNH_2 serving as sulfide source would release sulfide ions.

$$CH_3CSNH_2 + 3OH^- \rightarrow CH_3COO^- + NH_3 + S^{2-} + H_2O \quad (1)$$

Secondly, the amino-functionalized $LiNi_{0.5}Mn_{1.5}O_4$ with positive charge could adsorb negatively-charged ions including S^{2-} ions. During the calcination process, metal salts, metal-sulfides and gas products correspondingly yield. After washing, the soluble metal salts are removed and the porous metal-sulfides framework is formed.

High rate capability and excellent cycling stability of the cathode material are crucial indicators for electric vehicles batteries and grid-scale electricity storage. To evaluate the effect of surface-sulfidization on the rate capability of the $LiNi_{0.5}Mn_{1.5}O_4$ composites, the cells are charged/discharged at different current rates from 0.5 to 6 C (1 C = 148 mA g^{-1}) shown in Fig. 4(a). Comparing to the pristine Li-$Ni_{0.5}Mn_{1.5}O_4$, S-$LiNi_{0.5}Mn_{1.5}O_4$ electrodes exhibit superior rate capability especially at high rate. The S-$LiNi_{0.5}Mn_{1.5}O_4$ electrode delivers a discharge capacity of 115.8 mAh g^{-1} while the pristine electrode shows only 98.4 mAh g^{-1} at 6 C. The long-term cycling performance of a cathode material is always highly desirable for practical applications. Fig. 4(b) shows the long-life performances of $LiNi_{0.5}Mn_{1.5}O_4$ and S-Li-$Ni_{0.5}Mn_{1.5}O_4$ electrodes at 2 C. Obviously, the S-$LiNi_{0.5}Mn_{1.5}O_4$ demonstrates much better cyclic stability than that of the pristine one. After 2500 cycles, the S-$LiNi_{0.5}Mn_{1.5}O_4$ electrode delivers a capacity of 93.4 mAh g^{-1} with a retention rate of 74.9%. In contrast, the Li-$Ni_{0.5}Mn_{1.5}O_4$ electrode dropped from an initial 121.3 mAh g^{-1} to 54.9 mAh g^{-1} (45.3% of the initial capacity) merely after 1800 cycles. The improved electrochemical performances of S-$LiNi_{0.5}Mn_{1.5}O_4$ benefit from the hierarchically porous structure and enhanced electrical conductivity induced by surface-sulfidization. For example, heazlewoodite Ni_3S_2 with metallic nature should be responsible for the improved rate performances, which could significantly reduce the rate-induced polarization at high rate and facilitate rapid charge transfer during the electrochemical process [27,28]. The porous sulfidized-layer could not only suppress the undesired side reaction between Li-$Ni_{0.5}Mn_{1.5}O_4$ and the electrolyte, but also prevent CEI film peeling off from $LiNi_{0.5}Mn_{1.5}O_4$ particle, resulting in stable CEI film formed on cathode surface. In addition, the SiO_2-coating originating from APTES is also responsible for the improved cyclic stability by protecting Li-$Ni_{0.5}Mn_{1.5}O_4$ from HF attacking.

Fig. 5(a, b) shows the galvanostatic discharge capabilities of the pristine and S-$LiNi_{0.5}Mn_{1.5}O_4$ at various rates ranging from 0.5 C to 6 C. As can be found, the $LiNi_{0.5}Mn_{1.5}O_4$ electrode undergoes fast capacity fade as the current densities monotonically increase accompanying with significantly dropped discharge plateaus, which might be attributed to the increase in electrode overpotential and IR drop at high rates [29]. In comparison, the discharge profiles of the S-$LiNi_{0.5}Mn_{1.5}O_4$ electrode decline more slowly with less capacity and potential decay in the same process, indicating a smaller polarization of the electrodes. Even at 6C

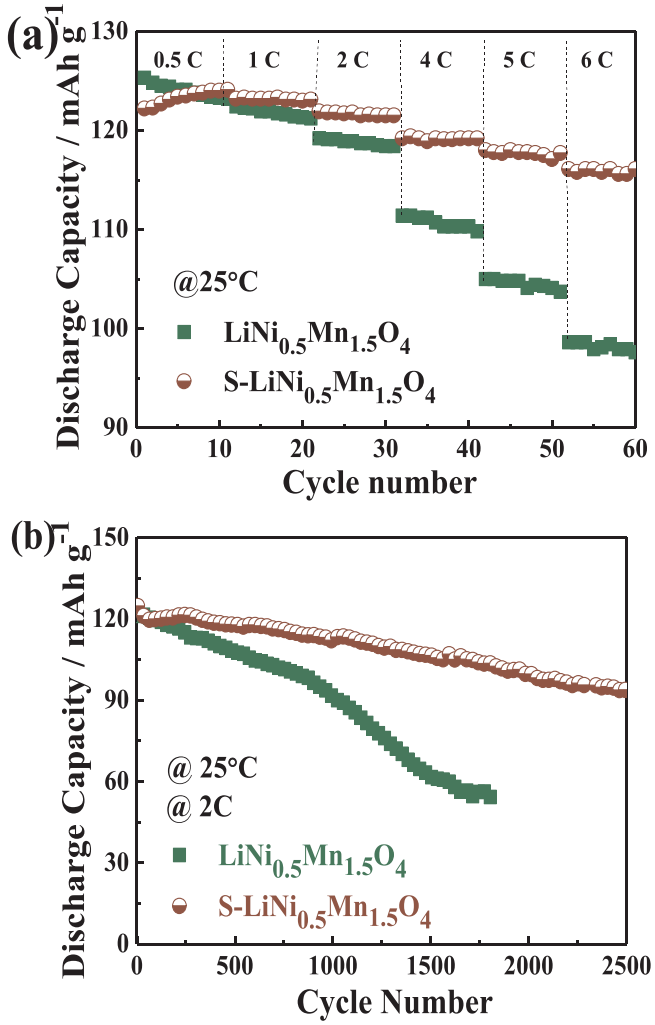

Fig. 4. (a) Rate capacity and (b) cycling performances of the pristine and surface-sulfidized $LiNi_{0.5}Mn_{1.5}O_4$ electrodes.

rate, an average discharging voltage of 4.52 V can be achieved for the S-$LiNi_{0.5}Mn_{1.5}O_4$ electrode, reflecting a good voltage character. The significant improvement in rate performance herein is mainly attributed to a faster Li^+ kinetics in $LiNi_{0.5}Mn_{1.5}O_4$ composite, which will be discussed later. Fig. S1(a, b) compared the discharge curves at different cycles for $LiNi_{0.5}Mn_{1.5}O_4$ and S-$LiNi_{0.5}Mn_{1.5}O_4$ electrodes at 2C. Compared to S-$LiNi_{0.5}Mn_{1.5}O_4$ electrodes, the voltage plateau of $LiNi_{0.5}Mn_{1.5}O_4$ declined at faster pace suggests a stronger polarization.

Fig. 5(c) shows the derivative plots dQ/dV at 105th cycle for the pristine and surface-sulfidized $LiNi_{0.5}Mn_{1.5}O_4$ electrodes. The two well-defined peaks around 4.7 V are ascribed to $Ni^{2+} \leftrightarrow Ni^{3+}$ and $Ni^{3+} \leftrightarrow Ni^{4+}$. The redox peaks in the 4.0 V region are assigned to the Mn^{3+}/Mn^{4+} redox reaction, indicating the presence of Mn^{3+} [30]. In comparison, S-$LiNi_{0.5}Mn_{1.5}O_4$ has a smaller difference in potential between redox pairs (ΔV) than that of the pristine one, further confirming that surface-sulfidization could effectively reduce the electrode polarization and promote the Li-ion transfer across the interface between $LiNi_{0.5}Mn_{1.5}O_4$ and electrolyte. Fig. 5(d) shows the electrochemical impedance measurements (EIS) of $LiNi_{0.5}Mn_{1.5}O_4$ and S-$LiNi_{0.5}Mn_{1.5}O_4$ electrodes at the full charge state. Both EIS curves are fitted based on the equivalent circuit in inset of Fig. 5(d), where Rs, Rsf, Rct, and Zw refer to the solution resistance, the surface layer resistance, the charge transfer resistance and Warburg impedance, respectively. The Rct values of the pristine and surface-sulfidized $LiNi_{0.5}Mn_{1.5}O_4$ electrodes are calculated as 710 and 250 Ω respectively. Lower charge transfer resistance reflects the mitigation of the CEI-layer growth, smaller interfacial resistance between active material and electrolyte, and a lower electrochemical polarization especially at high C-rate, which are in favor of the improvement of charge transfer kinetics through surface layer [31]. On the other hand, SO_4^{2-} adsorbed on the surfaces would enhance the coordination of the surface transition metal ions and form a more stable CEI layer, which can efficiently prevent electrolyte decomposition [32].

The surface morphologies of $LiNi_{0.5}Mn_{1.5}O_4$ and S-$LiNi_{0.5}Mn_{1.5}O_4$ particles after 150 galvanostatic charge/discharge cycles are compared in Fig. 6(a, b). It is clear that S-$LiNi_{0.5}Mn_{1.5}O_4$ has a more smooth surface morphology than that of $LiNi_{0.5}Mn_{1.5}O_4$ particle, indicating the protective nature of the sulfidized-layer against solvent oxidation for high-voltage $LiNi_{0.5}Mn_{1.5}O_4$ cathode. Tiny void spaces would exist at $LiNi_{0.5}Mn_{1.5}O_4$/electrolyte interface, which are induced by volume change of $LiNi_{0.5}Mn_{1.5}O_4$ associated with the repeated Li^+ insertion/extraction processes. Such void spaces hinder electrons to transfer across the interface and 3D surface-sulfidized network provides an alternative channel across the interface shown in Fig. 6(c). On the other hand, CEI film tends to peel off from the $LiNi_{0.5}Mn_{1.5}O_4$ surface because of the void spaces and the lattice mismatch between $LiNi_{0.5}Mn_{1.5}O_4$ and CEI film. 3-D porous structure of sulfidized-layer helps to fix tightly CEI film on $LiNi_{0.5}Mn_{1.5}O_4$ surface, reduce interfacial resistance for charge transfer across the $LiNi_{0.5}Mn_{1.5}O_4$/electrolyte interface, and consequently decrease energy barrier for Li-ions hopping.

To get insight into the influence of surface-sulfidization on the kinetics of Li-ion diffusion, the impedance spectra for $LiNi_{0.5}Mn_{1.5}O_4$ and S-$LiNi_{0.5}Mn_{1.5}O_4$ electrodes under different charge/discharge states are carried out. Based on the linear relationship between the real axis (Z′) and the reciprocal square root ($\omega^{-1/2}$) at low angular frequencies shown in Fig. S2, the chemical diffusion coefficient of Li^+ (D_{Li}^+) can be calculated as follows

$$Z' = R_e + R_{ct} + \sigma_\omega \omega^{-1/2} \quad (2)$$

$$D_{Li}^+ = \left(\frac{2RT}{\sqrt{2}n^2F^2\sigma_w AC}\right)^2 = \frac{2R^2T^2}{n^4F^4\sigma_w^2A^2C^2} \quad (3)$$

where R and T are the mass gas constant and absolute temperature respectively; F and A are Faraday's constant and the surface area of the electrode respectively; σ_w is the Warburg coefficient; n is the number of electrons per molecule during oxidation; C is the molar volume of active material. As shown in Fig. 6(d, e), both electrodes have three distinct peaks around 4.0 and 4.7 V, which are assigned to Mn^{3+}/Mn^{4+}, $Ni^{2+} \leftrightarrow Ni^{3+}$ and $Ni^{3+} \leftrightarrow Ni^{4+}$ redox reaction. In comparison, S-$LiNi_{0.5}Mn_{1.5}O_4$ electrodes demonstrate larger Li-ion diffusion coefficients than those of the $LiNi_{0.5}Mn_{1.5}O_4$ during the charge/discharge process. Higher diffusion coefficients indicate the better rate capability of S-$LiNi_{0.5}Mn_{1.5}O_4$ electrodes. It is expected that surface-sulfidized layer with porous structure would be in favor of CEI-film stability via reducing strain-induced interface degradation, mediate the increase in charge transfer resistance, facilitate Li-ion transfer across the electrode/electrolyte interface.

The stability of exposed crystal face should be mainly responsible for the stability of $LiNi_{0.5}Mn_{1.5}O_4$ electrode [33]. Fig. S3(a, b) presents the optimized structures of {1 1 1} $LiNi_{0.5}Mn_{1.5}O_4$ and S-$LiNi_{0.5}Mn_{1.5}O_4$ surface according to the DFT calculations, where SO_4^{2-}-ions are incorporated on {1 1 1} surface of surface-sulfidized $LiNi_{0.5}Mn_{1.5}O_4$. To get physical insight on the relationship between the electrochemical performance and structure of electrode material, the dissolution energy of Mn on {1 1 1} surface is investigated. Herein, the dissolution energy is calculated by:

$$E_{dissolution} = E_{surface} - E_{production} - \mu Mn \quad (4)$$

where $E_{surface}$ and $E_{product}$ are the total energy of fully relaxed surface structure and the total energy of fully relaxed product with one Mn atom dissociated. μMn refers to the chemical potential of Mn atom. It is

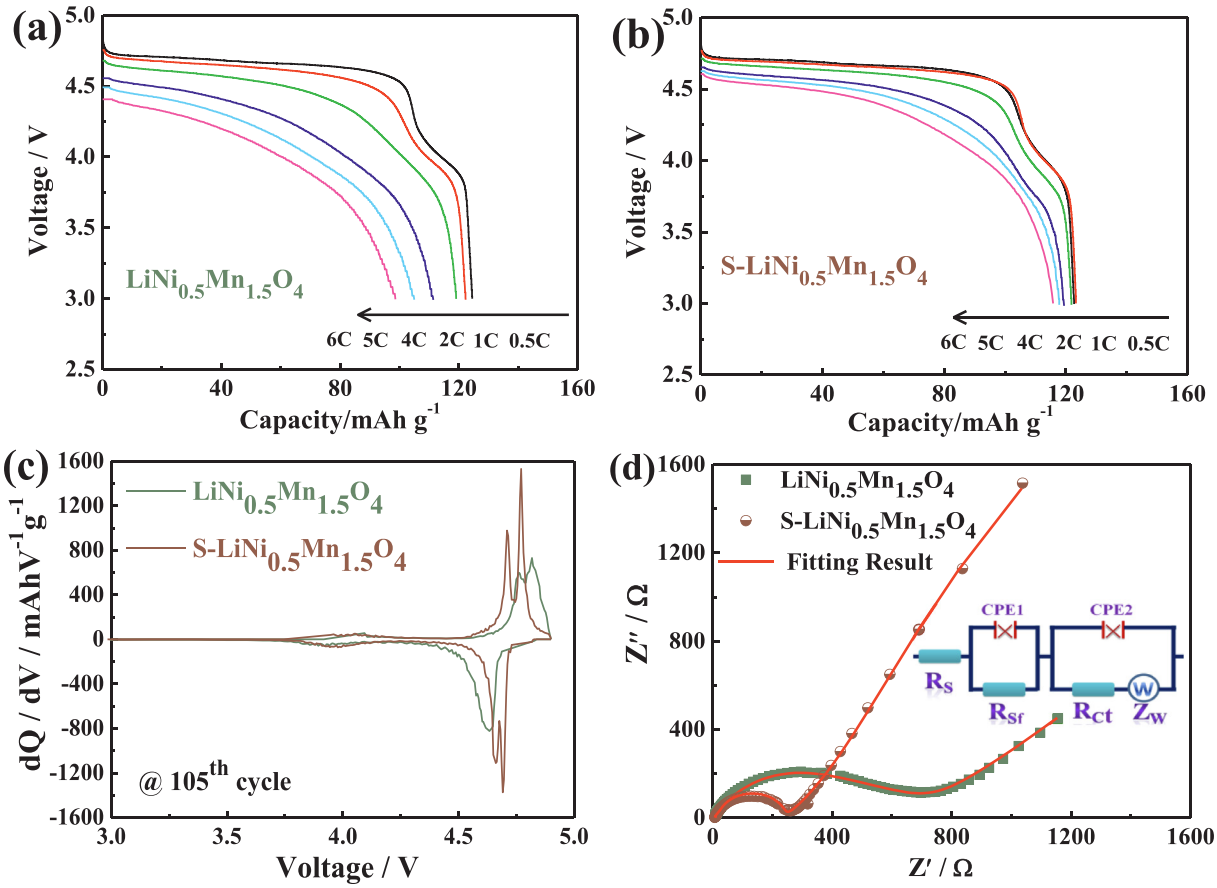

Fig. 5. (a,b) The galvanostatic discharge capabilities of the pristine and S-$LiNi_{0.5}Mn_{1.5}O_4$ at different C-rate; (c) Derivative plots dQ/dV at 105th cycle of the pristine and surface-sulfidized $LiNi_{0.5}Mn_{1.5}O_4$ electrodes; (d) EIS profiles and the corresponding equivalent circuit of the pristine and surface-sulfidized $LiNi_{0.5}Mn_{1.5}O_4$ electrodes.

found that S-$LiNi_{0.5}Mn_{1.5}O_4$ has higher $E_{dissolution}$ of {1 1 1} surface than that of the pristine one. The higher $E_{dissolution}$ after surface-sulfidization suggests the stronger ability to avoid the Mn dissolution, which is favorable for the enhanced cycling stability of $LiNi_{0.5}Mn_{1.5}O_4$ cathode.

The interfacial properties between $LiNi_{0.5}Mn_{1.5}O_4$ and electrolyte are crucial to the electrochemical performances and thermal stability of $LiNi_{0.5}Mn_{1.5}O_4$-based Li-ion batteries, which could be qualitatively characterized in terms of work function measured by Kelvin probe atomic force microscopy. The working electrodes including $LiNi_{0.5}Mn_{1.5}O_4$ and S-$LiNi_{0.5}Mn_{1.5}O_4$ powders (Fig. 7(a)) are galvanostatic charged/discharged and subsequently disassembled in an argon-filled glove box. Fig. S4(a-c) presents the surface potential maps across a scan area of 200 nm × 200 nm of $LiNi_{0.5}Mn_{1.5}O_4$, S-$LiNi_{0.5}Mn_{1.5}O_4$ and Au foil acting as calibrated sample. Based on our prior work [34], the work functions of $LiNi_{0.5}Mn_{1.5}O_4$ and S-$LiNi_{0.5}Mn_{1.5}O_4$ powders are calculated, shown in Fig. 7(b). S-$LiNi_{0.5}Mn_{1.5}O_4$ powders has a smaller work function (~5.68 eV) than that (~5.92 eV) of $LiNi_{0.5}Mn_{1.5}O_4$. The measured work function of $LiNi_{0.5}Mn_{1.5}O_4$ is close to the reported value [35,36]. According to the relative energies of the electrolyte window and the electrode electrochemical potentials, the electrolyte would be oxidized when the electrochemical potential (μ_C) of cathode is below the highest occupied molecular orbital (HOMO) of the electrolyte, as shown Fig. 7(c) [37,38]. Therefore, the oxidation of the electrolyte could be effectively suppressed by reducing the difference in work function between cathode material and the electrolyte. Hybrided by the metal-sulfides with smaller work function, the work function of the composite is reduced and the difference in work function is correspondingly reduced. As a result, the oxidation of the electrolyte could be effectively suppressed and the cycling capability of S-$LiNi_{0.5}Mn_{1.5}O_4$ is consequently improved.

After 150 galvanostatic charge/discharge cycles, S-$LiNi_{0.5}Mn_{1.5}O_4$ still exhibits a smaller work function than that of $LiNi_{0.5}Mn_{1.5}O_4$ shown in Fig. 7(d). The obtained results further confirm that surface-sulfidization would facilitate electron transfer in the composite and be beneficial for stable CEI-film via effectively suppressing electrolyte decomposition. Metal-sulfides such as metallic Ni_3S_2, embedding in CEI layer are desirable for electron transfer rather than insulating CEI film based on the scattering theory of electron transport across the interface [39]. Meanwhile, 3D porous framework of sulfidized-layer tends to fix CEI-film tightly and prevents CEI-film peeling off from cathode materials during the charging/discharging process. As a result, surface-sulfidized $LiNi_{0.5}Mn_{1.5}O_4$ electrode shows superior cycling stability and excellent rate capability. It is well-established that the oxidation of transition metal sulfides would occur at high voltage and Ni^{2+} is oxidized to Ni^{4+} in the process of charging to 4.9 V. When the cells are constant-voltage charged at 4.9 V for 120 min, NiS and NiS_2 beside Ni_3S_2 phases are found in the XRD pattern (Fig. S5), indicating that transition metals will be gradually oxidized to higher valence state at high voltage. Therefore, as the charging/discharging process proceeds, the sulfidized layer should contain NiS and NiS_2 besides other metal sulfides such as MnS_2, Ni_3S_2, Ni_3S_4. It has been reported that the resulted NiS and NiS_2 are have excellent conductivity [40], which could also facilitate electron transfer in the electrode.

The excellent thermal stability and safety of cathode materials are highly desirable for the large-scale practical applications. Fig. 7(e) shows differential scanning calorimetry (DSC) curves of $LiNi_{0.5}Mn_{1.5}O_4$ and S-$LiNi_{0.5}Mn_{1.5}O_4$ in a highly-delithiated state measured from 30 to 400 °C. $LiNi_{0.5}Mn_{1.5}O_4$ cathode shows two exothermic peaks at around

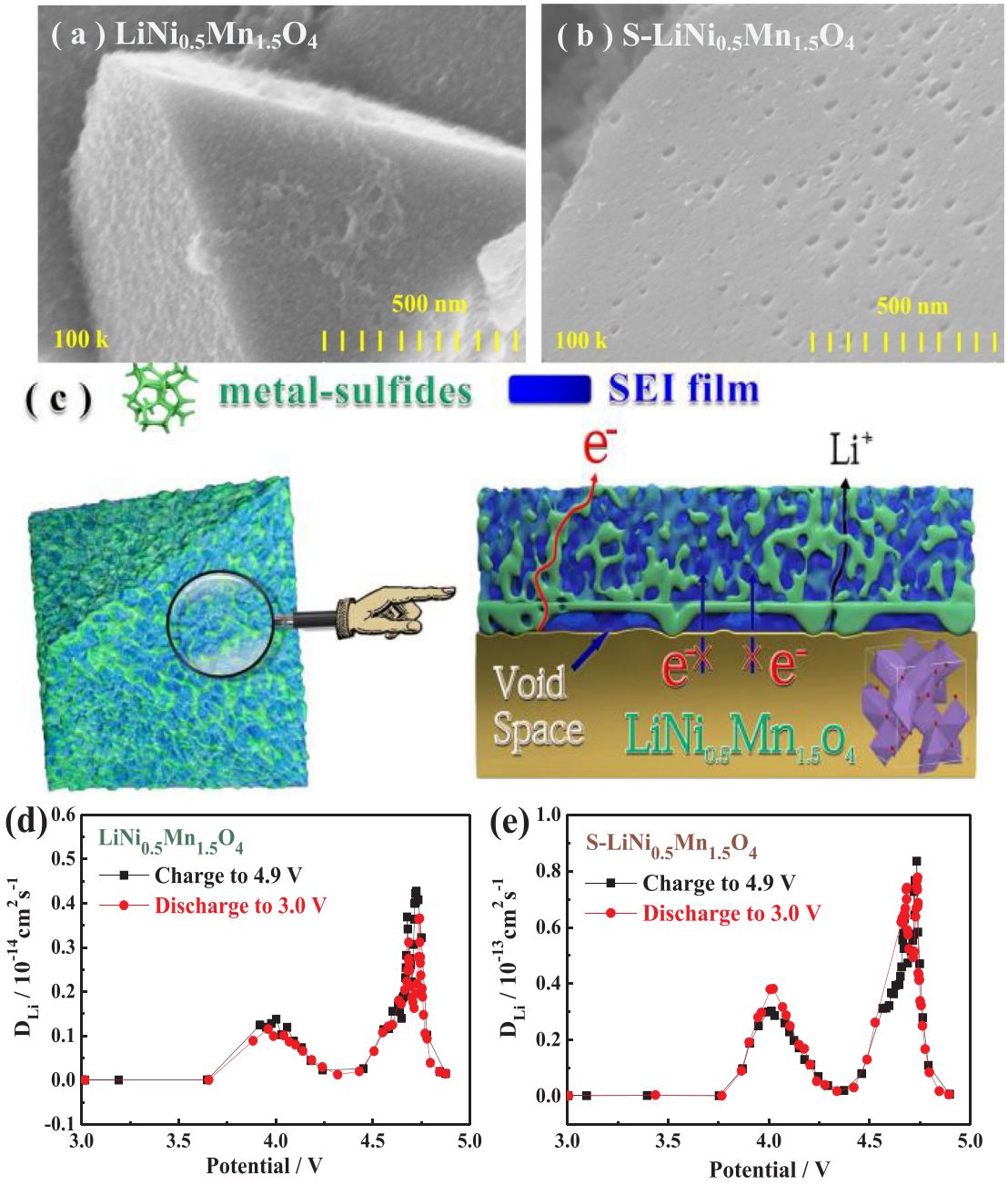

Fig. 6. (a,b) Surface morphologies of $LiNi_{0.5}Mn_{1.5}O_4$ and S-$LiNi_{0.5}Mn_{1.5}O_4$ after 150 cycles; (c) Potential mechanism behind the improved electrochemical performances after surface sulfidization; (d, e) Li-ion diffusion coefficients for $LiNi_{0.5}Mn_{1.5}O_4$ and S-$LiNi_{0.5}Mn_{1.5}O_4$ electrodes.

158.1 °C and 234.7 °C respectively. The exothermic behavior before 200 °C is related to the O_2-releasing and the one after 200 °C is related to the further oxidation reaction between electrolyte and active materials [41,42]. In comparison, S-$LiNi_{0.5}Mn_{1.5}O_4$ cathode exhibits less reaction enthalpy around 156.3 °C and the exothermic peak related to oxidation reaction is extended to 281.6 °C. The enhanced thermal stability is probably due to the surface-sulfidization layer suppressing the vigorous side reactions between highly oxidative $LiNi_{0.5}Mn_{1.5}O_4$ and liquid electrolyte.

The reduced work function of S-$LiNi_{0.5}Mn_{1.5}O_4$ is well explained phenomenologically using the energy-band model [34]. As shown in Fig. 8(a), electrons would transfer from the composite with smaller work function (MnS: 4.81 eV, MnS_2: 5.24 eV, Ni_3S_4: 4.97 eV, Ni_3S_2:5.11 eV, NiS:5.11 eV, NiS_2:5.0 eV) [43–46] to $LiNi_{0.5}Mn_{1.5}O_4$ with larger work function until the Fermi levels are aligned [47]. As a result, the Fermi levels of the composite is closer to the highest occupied molecular orbital (HOMO) of carbonate electrolyte (5.6 eV) [48], which effectively releases the oxidation of the electrolyte, facilitates Li-ion diffusion across the surface of the cathode material and consequently improves the thermodynamic stability of the cathode materials during the charge/discharge process. On the other hand, a built-in electric field (E) correspondingly forms between positively-charged metal-sulfides and negatively-charge $LiNi_{0.5}Mn_{1.5}O_4$ due to the electrons transfer, shown in Fig. 8 (b, c). Such electric field could facilitate Li-ion diffusion from metal-sulfides to $LiNi_{0.5}Mn_{1.5}O_4$, and electron transfer from Ni_3S_4 to $LiNi_{0.5}Mn_{1.5}O_4$ across heterojunction interfaces. As a result, the synergy effects among metal-sulfides on $LiNi_{0.5}Mn_{1.5}O_4$ surface would be favorable for Li-ion diffusion and electron transfer in the electrode during the lithium insertion process.

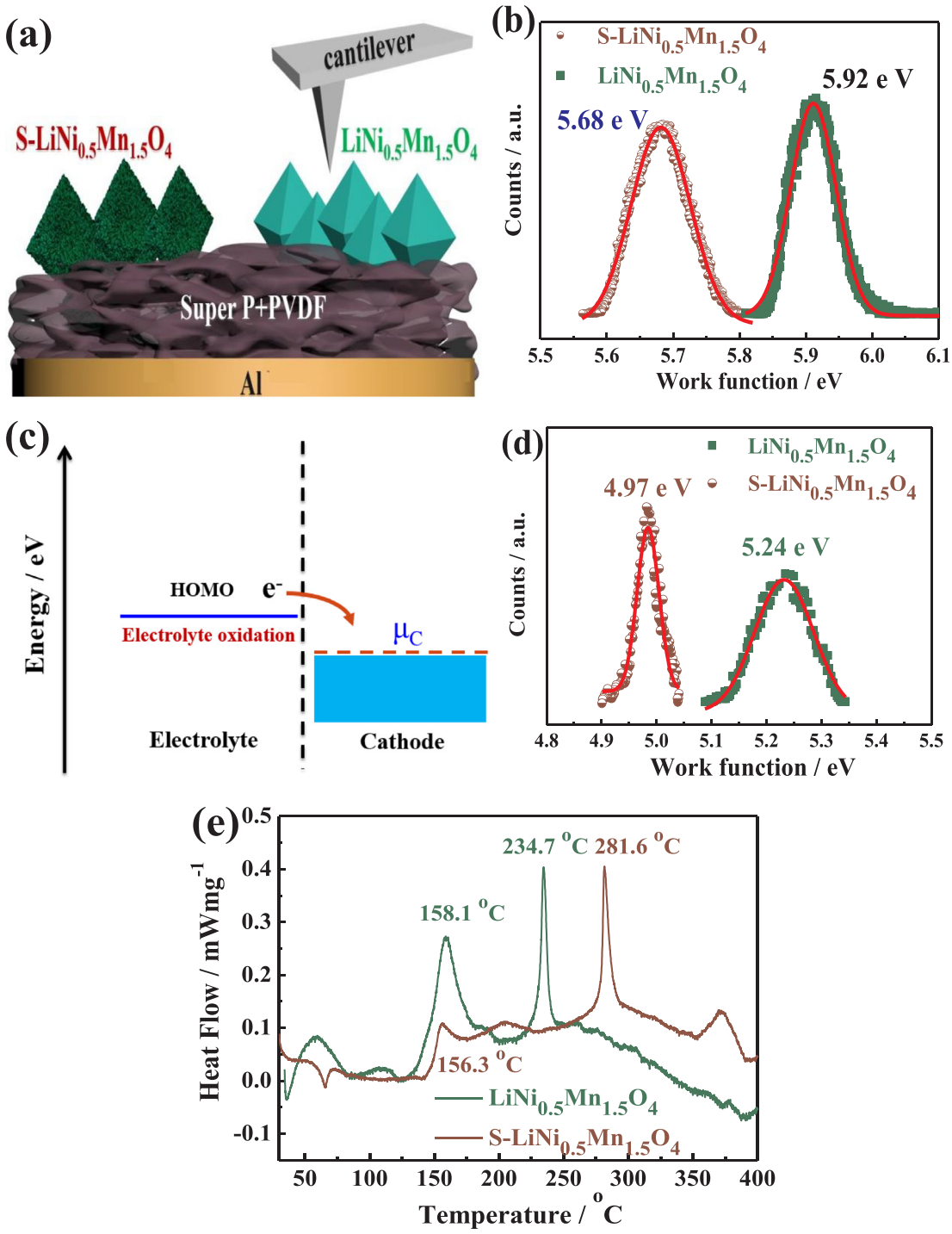

Fig. 7. (a) The working electrode for work function measurements; (b) work functions of fresh LiNi0.5Mn1.5O4 and S-$LiNi_{0.5}Mn_{1.5}O_4$ powders; (c) the relative energies of the electrolyte window and the electrochemical potentials of cathode material; (d) work functions of the pristine and surface-sulfidized $LiNi_{0.5}Mn_{1.5}O_4$ after 150 cycles; (e) DSC profiles of bare and surface-sulfidized $LiNi_{0.5}Mn_{1.5}O_4$ at full charged state.

4. Conclusions

In summary, we demonstrate an effective surface-sulfidization on $LiNi_{0.5}Mn_{1.5}O_4$ via electrostatic interactions. Surface-sulfidized $LiNi_{0.5}Mn_{1.5}O_4$ cathode exhibits superior cyclability, excellent rate capability and improved thermal stability. The distinctive advantage of the surface-sulfidization is the formation of a 3-dimensional porous sulfidized layer, which is favor of the formation of stable CEI film and the improvement in Li-ion diffusion kinetics through surface layer. Moreover, the adsorption of SO_4^{2-} on surface and reduced work function induced by surface-sulfidization, help to enhance $LiNi_{0.5}Mn_{1.5}O_4$/electrolyte interfacial stability and improve rate capability.

Declaration of Competing Interest

The authors declare that they have no known competing financial interests or personal relationships that could have appeared to influence the work reported in this paper.

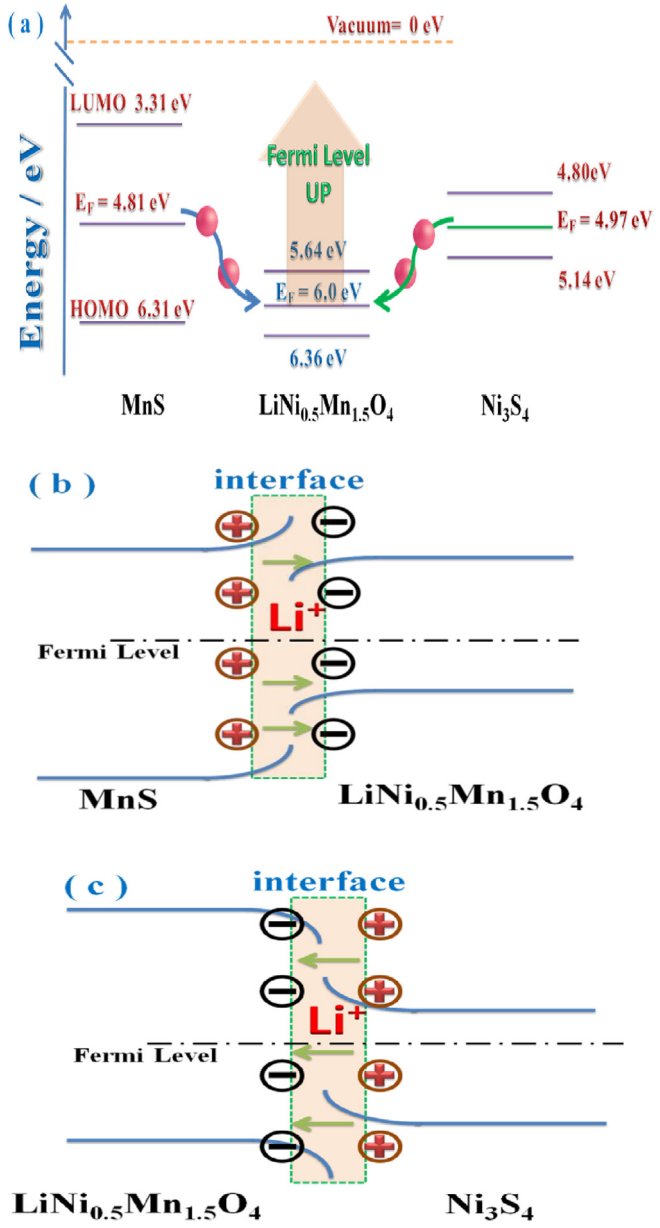

Fig. 8. (a) Energy-level model explaining the improved thermal stability; (b, c) a built-in electric field for charge transfer at heterojunction interface.

Acknowledgements

L. Y. Wei and J. M. Tao contributed equally to this work. This work is supported by a grant from Key Project of Department of Science & Technology of Fujian Province (No. 2014H0020) and Solar Energy Conversion & Energy Storage Engineering Technology Innovation Platform (No. 2018L3006).

Appendix A. Supplementary data

Supplementary data to this article can be found online at https://doi.org/10.1016/j.cej.2019.123268.

References

[1] J. Jaguemont, L. Boulon, Y. Dubé, A comprehensive review of lithium-ion batteries used in hybrid and electric vehicles at cold temperatures, Appl. Energy 164 (2016) 99–114.
[2] J.W. Choi, D. Aurbach, Promise and reality of post-lithium-ion batteries with high energy densities, Nat. Rev. Mater. 1 (2016) 16013–16028.
[3] P.K. Nayak, E.M. Erickson, F. Schipper, T.R. Penki, N. Munichandraiah, P. Adelhelm, H. Sclar, F. Amalraj, B. Markovsky, D. Aurbach, Review on challenges and recent advances in the electrochemical performance of high capacity Li- and Mn-rich cathode materials for Li-ion batteries, Adv. Energy Mater. 8 (2018) 1702397.
[4] J.L. Shi, D.D. Xiao, M.Y. Ge, X.Q. Yu, Y. Chu, X.J. Huang, X.D. Zhang, Y.X. Yin, X.Q. Yang, Y.G. Guo, L. Gu, L.J. Wan, High-capacity cathode material with high voltage for Li-ion batteries, Adv. Mater. 30 (2018) 1705575.
[5] A. Manthiram, K. Chemelewski, E.S. Lee, A perspective on the high-voltage $LiMn_{1.5}Ni_{0.5}O_4$ spinel cathode for lithium-ion batteries, Energy Environ. Sci. 7 (2014) 1339–1350.
[6] F. Wang, L.M. Suo, Y.J. Liang, C.Y. Yang, F.D. Han, T. Gao, W. Sun, C.S. Wang, Spinel $LiNi_{0.5}Mn_{1.5}O_4$ cathode for high-energy aqueous lithium-ion batteries, Adv. Energy Mater. 7 (2017) 1600922.
[7] W.W. Sun, Y.J. Li, Y.M. Liu, Q.P. Guo, S.Q. Luo, J.G. Yang, C.M. Zheng, K. Xie, Hierarchical waxberry-like $LiNi_{0.5}Mn_{1.5}O_4$ as an advanced cathode material for lithium-ion batteries with a superior rate capability and long-term cyclability, J. Mater. Chem. A 6 (2018) 14155–14161.
[8] T. Hwang, J.K. Lee, J. Mun, W. Choi, Surface-modified carbon nanotube coating on high-voltage $LiNi_{0.5}Mn_{1.5}O_4$ cathodes for lithium ion batteries, J. Power Sources 322 (2016) 40–48.
[9] S. Nageswaran, M. Keppeler, S.J. Kim, M. Srinivasan, Morphology controlled Si-modified $LiNi_{0.5}Mn_{1.5}O_4$ microspheres as high performance high voltage cathode materials in lithium ion batteries, J. Power Sources 346 (2017) 89–96.
[10] L.B. Ben, H.L. Yu, Y.D. Wu, B. Chen, W.W. Zhao, X.J. Huang, Ta_2O_5 coating as an HF barrier for improving the electrochemical cycling performance of high-voltage spinel $LiNi_{0.5}Mn_{1.5}O_4$ at elevated temperatures, ACS Appl. Energy Mater. 1 (2018) 5589–5598.
[11] J. Wang, P. Nie, J.M. Jiang, Y.T. Wu, R.R. Fu, G.Y. Xu, Y.D. Zhang, H. Dou, X.G. Zhang, High-voltage Li_2SiO_3-$LiNi_{0.5}Mn_{1.5}O_4$ hollow spheres prepared through in situ aerosol spray pyrolysis towards high-energy Li-ion batteries, ChemElectroChem. 5 (2018) 1212–1218.
[12] T.H. Xu, Y.P. Li, D.D. Wang, M.Y. Wu, D. Pan, H.L. Zhao, Y. Bai, Enhanced electrochemical performance of $LiNi_{0.5}Mn_{1.5}O_4$ cathode material by YPO_4 surface modification, ACS Sustainable Chem. Eng. 5 (2018) 5818.
[13] Z.H. Chen, Y. Qin, K. Amine, Y.K. Sun, Role of surface coating on cathode materials for lithium-ion batteries, J. Mater. Chem. 20 (2010) 7606–7612.
[14] W. Liu, X.F. Li, D.B. Xiong, Y.C. Hao, J.W. Li, H.R. Kou, B. Yan, D.J. Li, S.G. Lu, A. Koo, K. Adair, X.L. Sun, Significantly improving cycling performance of cathodes in lithium ion batteries: the effect of Al_2O_3 and $LiAlO_2$ coatings on $LiNi_{0.6}Co_{0.2}Mn_{0.2}O_2$, Nano Energy 44 (2018) 111–120.
[15] L. Wen, X.W. Wang, G.Q. Liu, H.Z. Luo, J. Liang, S.X. Dou, Novel surface coating strategies for better battery materials, Surf. Inno. 6 (2018) 13.
[16] W.W. Sun, Y.J. Li, K. Xie, S.Q. Luo, G.X. Bai, X.J. Tian, C.M. Zheng, Constructing hierarchical urchin-like LiNi0.5Mn1.5O4 hollow spheres with exposed 111 facets as advanced cathode material for lithium-ion batteries, Nano Energy 54 (2018) 175–183.
[17] L.L. Li, T. Tian, J. Jiang, L.H. Ai, Hierarchically porous Co_3O_4 architectures with honeycomb-like structures for efficient oxygen generation from electrochemical water splitting, J. Power Sources 294 (2015) 103–111.
[18] F.D. Yu, L.F. Que, Z.B. Wang, Y. Xue, Y. Zhang, B.S. Liu, D.M. Gu, Controllable synthesis of hierarchical ball-in-ball hollow microspheres for a high performance layered Li-rich oxide cathode material, J. Mater. Chem. A 5 (2017) 9365–9376.
[19] J. Wang, P. Nie, G.Y. Xu, J.M. Jiang, Y.T. Wu, R.R. Fu, H. Dou, X.G. Zhang, High-voltage $LiNi_{0.45}Cr_{0.1}Mn_{1.45}O4$ cathode with superlong cycle performance for wide temperature lithium-ion batteries, Adv. Funct. Mater. 24 (2018) 1704808.
[20] Q.J. Che, N.N. Bai, Q. Li, X.H. Chen, Y. Tan, X. Xu, One-step electrodeposition of a hierarchically structured S-doped NiCo film as a highly-efficient electrocatalyst for the hydrogen evolution reaction, Nanoscale 10 (2018) 15238–15248.
[21] H.T. Du, R.M. Kong, F.L. Qu, L.M. Lu, Enhanced electrocatalysis for alkaline hydrogen evolution by Mn doping in a Ni_3S_2 nanosheet array, Chem. Commun. 54 (2018) 10100–10103.
[22] Y.L. Bai, Z.H. Li, B.W. Cheng, M.L. Zhang, K.M. Su, Higher UV-shielding ability and lower photocatalytic activity of TiO_2@SiO_2/APTES and its excellent performance in enhancing the photostability of poly(p-phenylene sulfide), RSC Adv. 7 (2017) 21758–21767.
[23] J.H. Kim, S.T. Myung, C.S. Yoon, S.G. Kang, Y.K. Sun, Comparative study of LiNi0.5Mn1.5O4-δ and LiNi0.5Mn1.5O4 cathodes having two crystallographic structures: Fd3m and P4332, Chem. Mater. 16 (2004) 906–914.
[24] C. Cheng, D.C. Kong, C.Z. Wei, W.M. Du, J.B. Zhao, Y.Q. Feng, Q.L. Duan, Self-template synthesis of hollow ellipsoid Ni-Mn sulfides for supercapacitors, electrocatalytic oxidation of glucose and water treatment, Dalton Trans. 46 (2017) 5406–5413.
[25] S.M. Ji, L.G. Zhang, L.T. Yu, X.J. Xu, J. Liu, In situ carbon-coating and Ostwald ripening-based route for hollow Ni_3S_4@C spheres with superior Li-ion storage performances, RSC Adv. 6 (2016) 101752–101759.
[26] V.S. Kumbhar, Y.R. Lee, C.S. Ra, D. Tuma, B.K. Min, J.J. Shim, Modified chemical synthesis of MnS nanoclusters on nickel foam for high performance all-solid-state asymmetric supercapacitors, RSC Adv. 7 (2017) 16348–16359.
[27] Q.L. Liu, L.Z. Wei, Q.C. Liu, G.L. Chen, X.K. Kong, Anion engineering on 3D Ni_3S_2 nanosheets array toward water splitting, ACS Appl. Energy Mater. 1 (2018) 3488.
[28] L.L. Feng, G.T. Yu, Y.Y. Wu, G.D. Li, H. Li, Y.H. Sun, T. Asefa, W. Chen, X.X. Zou, High-index faceted Ni_3S_2 nanosheet arrays as highly active and ultrastable electrocatalysts for water splitting, J. Am. Chem. Soc. 137 (2015) 14023–14026.
[29] J.C. Fang, Y.F. Xu, G.L. Xu, S.Y. Shen, J.T. Li, L. Huang, S.G. Sun, Fabrication of

densely packed $LiNi_{0.5}Mn_{1.5}O_4$ cathode material with excellent long-term cycleability for high-voltage lithium ion batteries, J. Power Sources 304 (2016) 15–23.
[30] J.C. Arrebola, A. Caballero, L. Hernan, M. Melero, J. Morales, E.R. CastelÍon, Electrochemical properties of $LiNi_{0.5}Mn_{1.5}O_4$ films prepared by spin-coating deposition, J. Power Sources 162 (2006) 606–613.
[31] J.R. Mou, Y.L. Deng, Z.C. Song, Q.J. Zheng, K.H. Lam, D.M. Lin, Excellent rate capability and cycling stability in Li^+-conductive Li_2SnO_3-coated $LiNi_{0.5}Mn_{1.5}O_4$ cathode materials for lithium-ion batteries, Dalton Trans. 47 (2018) 7020–7028.
[32] S.G. Woo, J.H. Han, K.J. Kim, J.H. Kim, J.S. Yu, Y.J. Kim, Surface modification by sulfated zirconia on high-capacity nickel-based cathode materials for Li-ion batteries, Electrochim. Acta 153 (2015) 115–121.
[33] K.R. Chemelewski, D.W. Shin, W. Li, A. Manthiram, Octahedral and truncated high-voltage spinel cathodes: the role of morphology and surface planes in electrochemical properties, J. Mater. Chem. A 1 (2013) 3347–3354.
[34] L.C. Chen, Y.M. Yang, Z.S. Wang, Z.Y. Lin, J.Y. Zhang, Q.L. Su, Y. Chen, W. Chen, Y.B. Lin, Z.G. Huang, Enhanced electrochemical performances and thermal stability of $LiNi_{1/3}Co_{1/3}Mn_{1/3}O_2$ by surface modification with YF_3, J. Alloy. Compd. 711 (2017) 462–472.
[35] D. Liu, W. Zhu, J. Trottier, C. Gagnon, F. Barray, A. Guerfi, A. Mauger, H. Groult, C.M. Julien, J.B. Goodenough, K. Zaghib, Spinel materials for high-voltage cathodes in Li-ion batteries, RSC Adv. 4 (2014) 154–167.
[36] X.H. Liang, M.H. Huang, Y.C. Zhao, H.J. Wu, Y.J. Wang, F.W. Tang, Structural and electronic properties of cation doping on the spinel LiMn2O4: a first-principles theory, Int. J. Electrochem. Sci. 11 (2016) 4611.
[37] J.B. Goodenough, K.S. Park, The Li-ion rechargeable battery: a perspective, J. Am. Chem. Soc. 135 (2013) 1167–1176.
[38] P. Peljo, H.H. Girault, Electrochemical potential window of battery electrolytes: the HOMO–LUMO misconception, Energy Environ. Sci. 11 (2018) 2306–2308.
[39] Y.B. Lin, Y. Lin, T. Zhou, G.Y. Zhao, Y.D. Huang, Z.G. Huang, Enhanced electrochemical performances of $LiFePO_4$/C by surface modification with Sn nanoparticles, J. Power Sources 226 (2013) 20–26.
[40] N. Jiang, Q. Tang, M.L. Sheng, B. You, D.E. Jiang, Y.J. Sun, Nickel sulfides for electrocatalytic hydrogen evolution under alkaline conditions: a case study of crystalline NiS, NiS_2, and Ni_3S_2 nanoparticles, Catal. Sci. Technol. 6 (2016) 1077–1084.
[41] Y.Y. Yu, J. Wang, P. Zhang, J.B. Zhao, A detailed thermal study of usual $LiNi_{0.5}Co_{0.2}Mn_{0.3}O_2$, $LiMn_2O_4$ and $LiFePO_4$ cathode materials for lithium ion batteries, J. Energy Storage 12 (2017) 37–44.
[42] Y. Baba, S. Okada, J. Yamaki, Thermal stability of Li_xCoO_2 cathode for lithium ion battery, Solid State Ionics 18 (2002) 311–316.
[43] Y. Xu, M.A.A. Schoonen, The absolute energy positions of conduction and valence bands of selected semiconducting minerals, Am. Mineral. 85 (2000) 543–556.
[44] L.L. Cheng, Y.Y. Hu, L. Ling, D.D. Qiao, S.C. Cui, Z. Jiao, One-step controlled synthesis of hierarchical hollow Ni_3S_2/NiS@Ni_3S_4 core/shell submicrospheres for high-performance supercapacitors, Electrochim. Acta 283 (2018) 664–675.
[45] Z.X. Qin, Y.B. Chen, Z.X. Huang, J.Z. Su, Z.D. Diao, L.J. Guo, Composition-dependent catalytic activities of noble-metal-free NiS/Ni_3S_4 for hydrogen evolution reaction, J. Phys. Chem. C 120 (2016) 14581–14589.
[46] M. Zervos, E. Leontidis, E. Tanas, E. Vasile, A. Othonos, Sn:In_2O_3 and Sn:In_2O_3/NiS_2 core–shell nanowires on Ni, Mo Foils and C fibers for H_2 and O_2 generation, J. Phys. Chem. C 121 (2017) 27839–27848.
[47] B. Bhushan, Scanning Probe Microscopy in Nanoscience and Nanotechnology, Springer Heidelberg, Dordrecht London New York, 2017, p. 46.
[48] J. Ma, P. Hu, G.L. Cui, L.Q. Chen, Surface and interface issues in spinel $LiNi_{0.5}Mn_{1.5}O_4$: insights into a potential cathode material for high energy density lithium ion batteries, Chem. Mater. 28 (2016) 3578–3606.